Journal of Advanced Electrochemical Storage

ISSN (Online): 3139-7190

Indexed in www.pubj.org



Role of induced strain on the optical properties of MOF (MIL-125)-derived Fe-doped TiO_2 material

Tholkappiyan Ramachandran[1,*]

[1]*Department of Physics, College of Science, United Arab Emirates University, Al-Ain, Abu Dhabi, P. O. Box 15551, United Arab Emirates.*

*Corresponding author: thols2006@gmail.com

DOI: https://doi.org/10.67977/jaes.vol.2.issue1.3

J. Adv. Electro. Storage 2(1) 2026 144–149



Keywords: MOF; Fe-doped TiO_2; Solvothermal reaction; X-ray diffraction; optical properties.

Received 11th May 2026
Published 14th June 2026

Licensed under CC-BY 4.0



ABSTRACT: In this work, we reported a facile and solvothermal strategy for synthesizing pristine and Fe-doped TiO_2 nanocrystalline materials through the metal-organic framework (MIL-125) route. Various characterization techniques are used to analyze the properties of the resultant nanocrystalline materials, including XRD, Raman, SEM, EDS, and UV-Vis spectroscopy techniques. X-ray diffraction and Raman studies of both samples confirm a tetragonal structure with an anatase phase with an average crystallite size of 35 and 43 nm and strain of 6.5 and 6.9 (line/m^2x10^{15}) from Williamson-Hall analysis. According to a morphological study, samples of TiO_2 are constructed into disc-like shapes, whereas Fe-doped TiO_2 is generated in cuboids. The optical band gap energies ranged from 3.3 eV to 2.2 eV. We were able to conclude that the produced strains had an impact on the optical band gap energies. Therefore, tweaking the optical properties in pristine and Fe-doped TiO_2 samples can be achieved.

1. INTRODUCTION

Supermolecule-scale atoms and molecules are the focus of nanotechnology. The physical and chemical properties of nanomaterials change dramatically at this level owing to the increasing surface-to-volume ratios [1]. In particular TiO_2 nanoparticles are widely used as a semiconductor material due to their main features, which include inexpensive, adequate oxidizing strength, superior chemical stability, high refractive index, and the presence of oxygen-containing functional groups in its lattice [2]. TiO_2 is a fine, white powder with no smell and is naturally hydrophobic under most circumstances. The most effective solar collectors are TiO_2 nanoparticles, which can capture 3-4% of solar energy [3]. It also has beneficial qualities like a broad bandgap and a hydrophobic nature. Industrial uses include textiles, dye-sensitized solar cells, self-cleaning, charge-spreading gadgets, sensors, electrochemistry, microelectronics, antimicrobial items, and photocatalysis [4,5]. Sol-gel, co-precipitation, citrate acetate precursor, combustion, ball milling, mechanochemical, hydrothermal, wet milling, and solid-state reaction are the usual techniques for making zinc ferrite nanoparticles [6]. However, some of these techniques are typically expensive, time-consuming, unreliable, and difficult to produce on a massive scale.

TiO_2 nanomaterials made of metal-organic frameworks (MOFs) have gained a lot of interest because of their benefits in structural engineering, such as their high porosities and remarkable variability [7]. A unique family of porous materials known as MOFs is composed of metal cations and organic linkers. It can be used as an effective template to build hierarchically porous metal

How to cite this article: Tholkappiyan Ramachandran. (2026). Role of induced strain on the optical properties of MOF (MIL-125)-derived Fe-doped TiO_2 material, Journal of Advanced Electrochemical Storage, 2(1), 144–149. https://doi.org/10.67977/vol.2.issue1.3

oxide nanostructures for various practical applications [8]. These metal oxides from MOFs frequently have accurate geometries, large porosities, simple heteroatom doping techniques, and metal nanoparticles. Significant multi-functional properties that are inherent to the precursor MOF employed can be found in them [9].

The current study focuses on facile and solvothermal strategies to synthesize the pristine and Fe-doped TiO_2 nanocrystalline materials through the MOF route. A complete evaluation of synthesized materials and a comprehensive examination of the optical, morphological and structural characteristics of NPs are explored. This work aims to report the effects of induced strains via the MOF route on their structural, morphological, and optical properties.

2. Experimental

2.1. Chemicals

The following products were purchased from Sigma Aldrich: titanium (IV) butoxide (97%), N, N-dimethyl formamide (99.8%), iron (II) chloride hexahydrate (99.99%), terephthalic acid (98%), and absolute ethanol (98%) Deionized H_2O was employed for the synthesis procedure along with all the reagents, which were not further purified. The solvothermal process was conducted in a 100 ml autoclave made by Baoshishan with a PTFE liner.

2.2. *Synthesis of PT and FeT via MOF route*

Our prior study described the synthesis process in detail, and it is as follows [10]. A facile solvothermal technique was used to create Ti-based metal-organic frameworks (MIL-125). Butyl titanate (1.56 ml) was progressively poured into a combination of 3g-terephthalic acid, 6 ml-anhydrous methanol and N, N-dimethyl methanamide (54 ml) while being constantly stirred for 10 minutes. The mixture is then put into a 100 ml stainless steel autoclave lined with Teflon and heated for 24 hours at 150 C. After the solvothermal process, the MOF (MIL-125) was carefully separated and produced in a white suspension by being washed repeatedly with methanol. The sample is dried for 12 hours at 80 C in a vacuum oven. The white precipitate produced by the solvothermal reaction was heat treated at 400 °C for 5 hours. 50 mg of $FeCl_26H_2O$ was additional to the reaction solution and a similar preparation technique was used to create the doped TiO_2 materials. The created materials were then kept for later examination and labeled as PT for undoped TiO_2 and FeT for Fe50%-doped TiO_2.

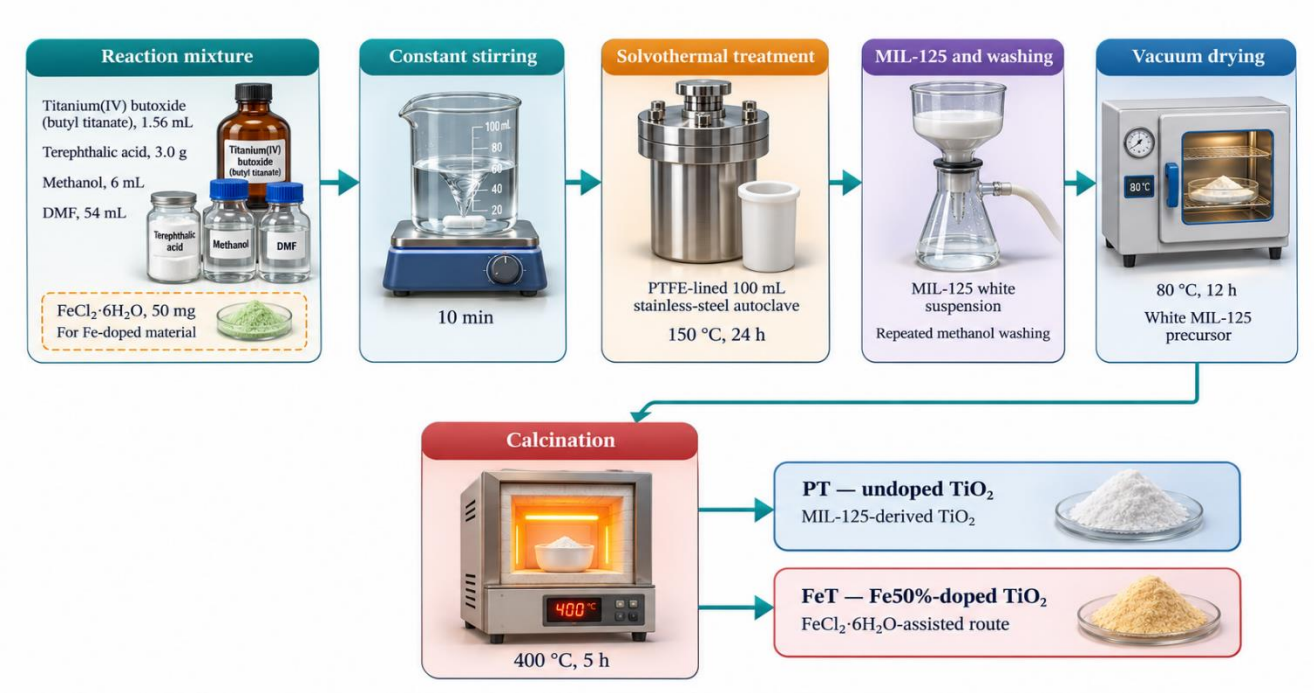


Figure 1. Schematic illustration of the solvothermal synthesis of MIL-125-derived TiO_2 (PT) and Fe 50%-doped TiO_2 (FeT).

2.2. *Materials characterization*

The phase identification was performed using Pan-analytical-Empyrean X-ray equipment with Cu Kα radiation at 45 kV over 10 to 80° diffraction angles. The International Centre for Diffraction Data (ICDD) database's standard patterns were used to identify the phase. A FEX-u confocal microscope Raman/PL system with a 532 nm excitation wavelength was used to measure Raman spectra over 100-1000 cm^{-1}. The Tecnai G2 F20 equipment from FEI, Netherlands, running at 20 kV, was used to conduct FESEM investigations.

3. RESULTS AND DISCUSSION

3.1. *Structural analysis*

The structural XRD investigations were used to analyze the phase development of the produced PT and FeT samples. The XRD pattern of room-temperature PT and FeT samples is depicted in Fig. 2. The 2θ angles about at 25.33, 37.78, 48.27, 55.02, 62.85, 70.14, and 75.46°, which are fitted to (101), (004), (200), (211), (204), and (215) to crystal planes, are connected to a tetragonal structure with an anatase phase of TiO_2 material, agreeing to JCPDS-21-1272 [11]. All the samples XRD peaks showed strong, sharp peaks, indicating the materials good crystalline character. The rise in the surface-to-volume ratio of the samples is also indicated by the peak broadening in the XRD plot. The purity of the synthesized samples is demonstrated by the absence of additional impurity peaks from any precursor or other oxide species. By using the Scherrer method, the typical average grain sizes, D_{avg} was calculated using the below formula [12],

$$D_{avg} = 0.9\lambda/\beta\cos\theta \quad (1)$$

Where λ denotes the X-ray wavelength (Å), D_{avg} represents the average grain size, β represents the full width at half maximum, and θ is the Bragg's angle. The predicted D_{avg} for the synthetic PT and FeT materials ranged between 35 and 43 nm. When compared to those for TiO_2 material, the value is favorable. [13].

.

Following Fe ion doping in TiO_2, it is evident from the recorded XRD pattern that the peak strength and width of the diffraction peaks decrease, which is connected to the lattice constants and is further examined by the Williamson-Hall method [14]. Typically, this method is an integral breadth method in which a Lorentzian curve is fitted to all the diffraction peak widths as a function of 2 Theta and FWHM. The strain and grain size have been calculated using a Williamson-Hall equation [12],

$$\beta\cos\theta = 0.9\lambda/ Davg + 4\varepsilon\sin\theta \quad (2)$$

Where ε is the lattice strain, Fig. 3 shows the Williamson-Hall plots by plotting 4 sinθ Vs β cosθ for all prominent peaks and applying linear best fitting. The graph's slope denotes lattice strain, and the intercepts reciprocal depicts the typical grain size. The computed grain size and strain, which are 32 and 38 nm and 6.5 and 6.9 (line/m^2x10^{15}), respectively, are in good agreement with the material's given parameters.

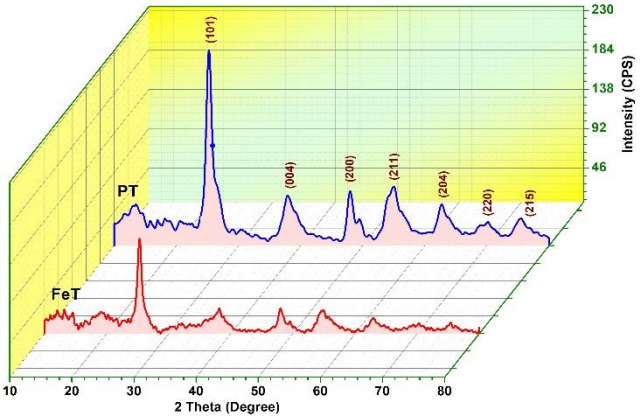


Figure 2 XRD pattern of the synthesized PT and FeT samples via the metal-organic framework (MOF) route.

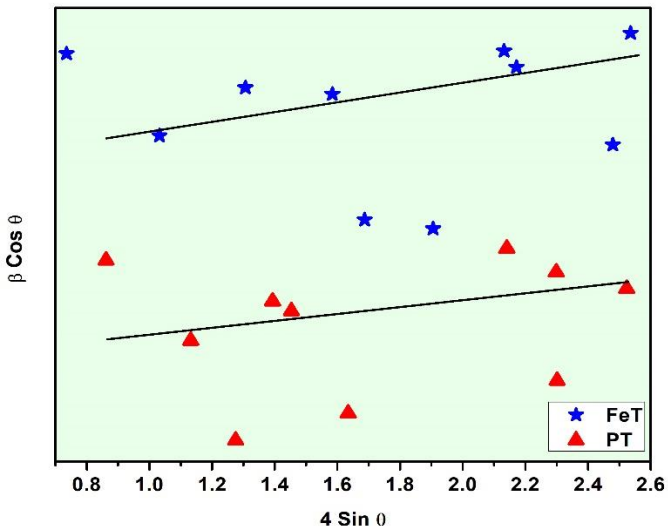


Figure 3 Williamson-Hall plot of the synthesized PT and FeT samples via the metal-organic framework (MOF) route.

3.2. Raman spectroscopy studies

More insights into the local structure of TiO_2 and the doping-induced structural changes can be understood deeply by Raman spectroscopy analysis. Fig. 4 shows the Raman spectra of PT and FeT samples. All spectra illustrate the formation of the anatase TiO_2 crystal structure. As observed in XRD, the Raman spectra also confirm the absence of any impurity and secondary peaks. The sharp, intense peak obtained at 144 cm^{-1} corresponds to the characteristic Eg mode of anatase TiO_2 that arises by symmetric stretching vibrations of O-Ti-O bonds. A low-intensity (Eg) peak was observed at 197 cm^{-1}. Apart from these, the peaks were obtained at 399, 518.9, and 643.74 cm^{-1}, which corresponds to B_{1g}, A_{1g}, or B_{1g} and E_g modes; in which B_{1g} mode arises by symmetric bending and A_{1g} mode by anti-symmetric bending vibrations of O–Ti–O bonds [15]. Any Raman modes are associated with stretching or bending vibration of Ti-O bonds. The Fe-doped samples exhibit approximately the same bands as the PT sample, and the results are consistent with XRD data. No prominent peaks related to the rutile phase were detected, confirming that the anatase phase of TiO_2 mostly dominated all samples.

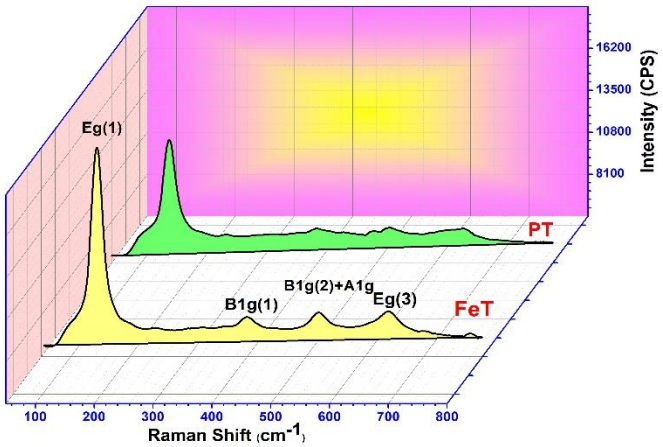


Figure. 4. Raman spectra in the 100–800 cm^{-1} for the synthesized PT and FeT samples.

3.3. Scanning electron microscopy

The FESEM micrographs of the synthesized MOF-derived PT and FeT electrode material are displayed in Fig. 5 (a-d). The detailed morphological topographies of the sample before and after Fe doping displayed substantial variations in size and shape. The PT sample (Fig. 5b) displayed disc-like shapes of different sizes (100-400 nm). The surface of the samples was found to be very rough, with large pores formed by the interconnected nano-crystallites. Fig. 5d depicts the 50wt% Fe-doped TiO_2 samples, respectively. After the doping, the average size of Fe-doped samples was increased to 1-3 µm. Iron doping caused the formation of cuboid morphology and is constructed by many tiny nanoparticles and has a highly porous structure, as observed in Fig. 5d.

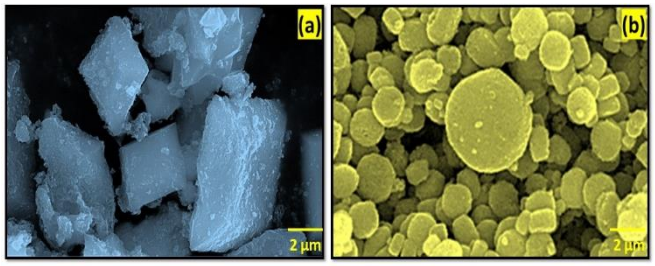


Figure. 5. FESEM micrographs with 2 µm of the synthesized MOF-derived TiO_2 (PT) (a) and FeT (b) samples.

3.4. Energy Dispersive X-Ray (EDS) analysis

The elemental analysis of the synthesized MOF-derived PT and FeT electrode material is displayed in Fig. 6(a-d). The EDS spectra show the existence of Ti, Fe, and O elements as shown in Fig. 6(a,c). No other elements were detected within the limits of our detector. This indicates the purity of PT and FeT samples.

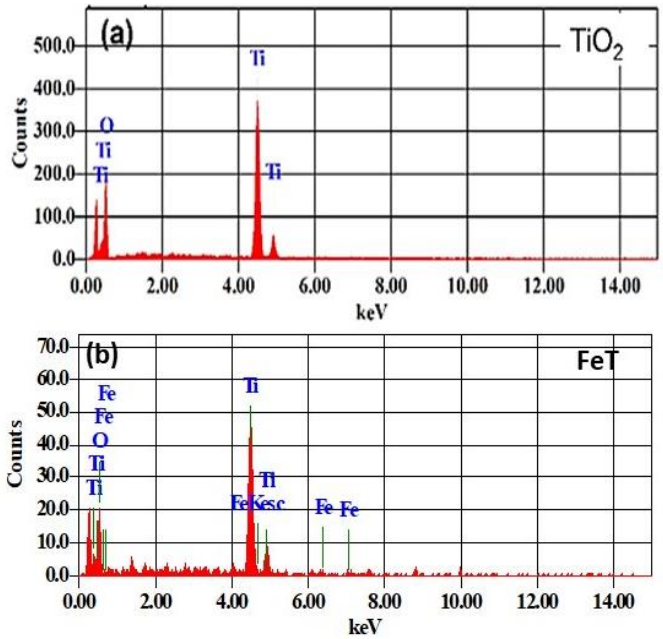


Figure. 6. EDS spectrum of the synthesized MOF-derived TiO_2 (PT) (a) and FeT (b) samples.

3.5. UV-Diffuse reflectance spectroscopy analysis

The bandgap may change if iron is included in the TiO_2 crystal lattice. Diffuse reflectance spectroscopy, as is shown in Fig. 7&8, can be used to identify this difference in bandgap following the integration of iron. The entire UV-vis spectral range is covered. Iron-doped TiO_2 samples showed more peaks in the visible limit (450–800) than in the pure sample [16]. Doping directly affects TiO_2's optical characteristics, extending light absorption into the visible spectrum owing to the emergence of sub-bandgap regions with oxygen vacancy sites between the conduction and valence bands. In the visible band (400–800 nm), the UV–vis diffuse reflection spectra of pure TiO_2 are perfectly flat. However, iron doping significantly reduces reflection. The bandgap energy is calculated using diffuse reflectance spectra per the hypothesis by P. Kubelka and F. Munk. The optical bandgap was reduced gradually from 3.3 to 2.2 eV, as shown in Table 1.

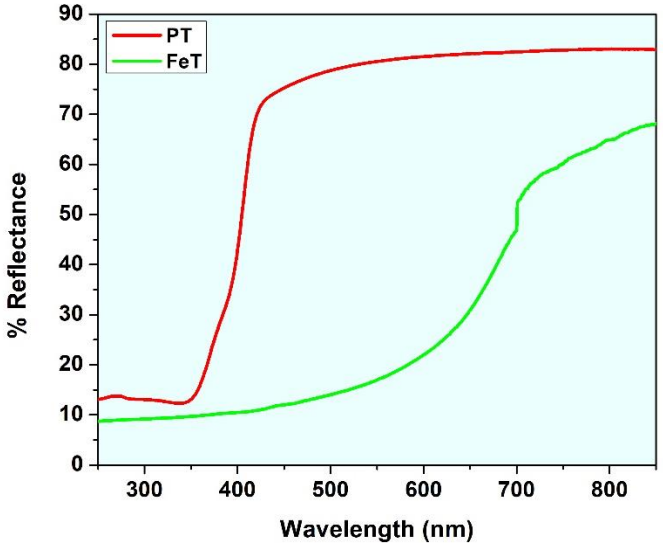


Figure. 7. Diffuse reflectance spectra of the synthesized MOF-derived TiO_2 (PT) (a) and FeT (b) samples.

Table 1: Structural and optical parameters of synthesized MOF-derived TiO_2 (PT) (a) and FeT (b) samples.

Sample	Band gap (eV)	Average crystalline size	Strain(line/ m^2x10^{15})
TiO_2	3.3	8.29	6.5
Fe-TiO_2	2.2	6.35	6.9

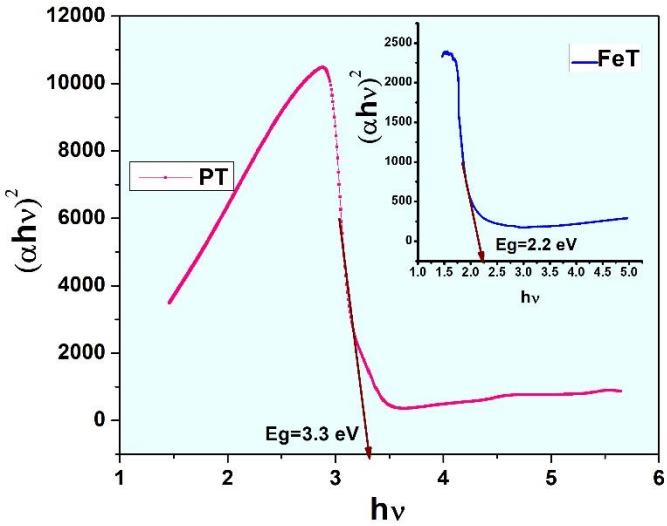


Figure. 8. Bandgap energy Kubelka–Munk plot of the synthesized MOF-derived TiO_2 (PT) (a) and FeT (b) samples.

4. CONCLUSION

In conclusion, a facile metal-organic framework route successfully synthesized the pristine and Fe-doped TiO2 nanocrystalline powders. The formation of the anatase crystal structure of all the samples before and after the dopant inclusion was confirmed by XRD, Raman, and HR-SEM analysis. However, they contained strains and led to an increase after Fe was doped. It was determined that the optical band gap energies vary from 3,3 eV to 2,2 eV. We concluded that the generated strains alter the optical band gap energies. Consequently, it is possible to modify the optical band gap in pure and Fe-doped TiO_2 nanocrystalline powders.

References

1. Valero-Romero, M. J., J. G. Santaclara, L. Oar-Arteta, L. Van Koppen, D. Y. Osadchii, Jorge Gascon, and Freek Kapteijn. "Photocatalytic properties of TiO2 and Fe-doped TiO2 prepared by metal organic framework-mediated synthesis." Chemical Engineering Journal 360 (2019): 75-88.
2. Yang, Huiying, Guangmin Ren, Zizhen Li, Zisheng Zhang, and Xiangchao Meng. "Fast Joule heating for transformation of Fe-MIL-125 (Ti) to Fe/TiO2 with enhanced photocatalytic activity in N2 fixation." Applied Catalysis B: Environment and Energy 347 (2024): 123795.
3. Yang, Tong-hui, Song Yue, Wei-wei Gong, Ren-qing Wang, Wei-da Hu, Xiao-pan Liu, Peng-zhao Gao, Hang Qin, Wen-ming Guo, and Han-ning Xiao.

"Mechanism of MOF-derived Fe-doped TiO2 material enhanced by the AC magnetic field on electrochemical nitrogen reduction reaction (eNRR)." International Journal of Hydrogen Energy 91 (2024): 447-457.

4. Liu, Tao, Aori Qileng, Nuermaimaitijiang Wubulikasimu, Zhixiong Liu, Weipeng Liu, and Yingju Liu. "Self-sacrificial templated synthesis of Fe/N Co-doping TiO2 for enhanced CO2 photocatalytic reduction." ChemNanoMat 9, no. 10 (2023): e202300343.
5. P. Nagaraju, A. Alsalme, A. Alswieleh, R. Jayavel, Facile in-situ microwave irradiation synthesis of TiO_2/graphene nanocomposite for high-performance supercapacitor applications, J. Electroanal. Chem., vol. 808, pp. 90–100, 2018.
6. Nizamudeen, C., R. Krishnapriya, Mohammad Sayem Mozumder, AH I. Mourad, and Tholkappiyan Ramachandran. "Photovoltaic performance of MOF-derived transition metal doped titania-based photoanodes for DSSCs." Scientific reports 13, no. 1 (2023): 6345.
7. Mishra, Dharmesh, Divya Rathore, Prapti Bansal, Mohit Garg, Surojit Pande, and Somak Chatterjee. "Novel Fe-doped TiO2 metal-organic framework for electrocatalytic hydrogen evolution reaction." Chemical Engineering Research and Design 207 (2024): 268-280.
8. Luo, Chao-Wei, Hao-Hua Huang, Xiong Jie, Di-Yang Peng, Chao-Rong Chen, and Hong-Yan Zeng. "Fe-doped NH2-MIL-125 (Ti) for enhanced photo-oxidation/reduction properties." Journal of Molecular Structure 1334 (2025): 141844.
9. Feng, Xuhui, Fuping Pan, Peng Zhang, Xiao Wang, Hong-Cai Zhou, Yongheng Huang, and Ying Li. "Metal-Organic Framework MIL-125 Derived Mg2+-Doped Mesoporous TiO2 for Photocatalytic CO2 Reduction." ChemPhotoChem 5, no. 1 (2021): 79-89.
10. R. Krishnapriya, C. Nizamudeen, B. Saini, M. S. Mozumder, R. K. Sharma, Abdel-Hamid I Mourad, MOF-derived Co^{2+}-doped TiO_2 nanoparticles as photoanodes for dye-sensitized solar cells. Sci. Rep., vol. 11, pp. 1–12, 2021.
11. Ahmed Alzamly, Fathalla Hamed, Tholkappiyan Ramachandran, Maram Bakiro, Salwa Hussein Ahmed, Shefaa Mansour, Sahar Salem, Nawf Saif Al Kaabi, Mohammed Meetani, Abbas Khaleel, Tunable band gap of Bi^{3+}-doped anatase TiO_2 for enhanced photocatalytic removal of acetaminophen under UV-visible light irradiation, Journal of Water Reuse and Desalination, vol. 9, pp. 31-46, 2019.
12. Wang, Libo, Shiyu Wang, Mohan Li, Xue Yang, Fengyan Li, Lin Xu, and Yongcun Zou. "Constructing oxygen vacancies and linker defects in MIL-125@ TiO2 for efficient photocatalytic nitrogen fixation." Journal of Alloys and Compounds 909 (2022): 164751.
13. Yao, Tianhao, Hongkang Wang, Yuanbin Qin, Jian-Wen Shi, and Yonghong Cheng. "Enhancing pseudocapacitive behavior of MOF-derived TiO2-x@ Carbon nanocubes via Mo-doping for high-performance sodium-ion capacitors." Composites Part B: Engineering 253 (2023): 110557.
14. Zhiliang Xiu, Muhammad Hilmy Alfaruqi, Jihyeon Gim, Jinju Song, Sungjin Kim, Trang Vu Thi, Pham Tung Duong, Joseph Paul Baboo, Vinod Mathew Jaekook Kim, Hierarchical porous anatase TiO_2 derived from a titanium metal–organic framework as a superior anode material for lithium-ion batteries. Chem. Commun., vol. 51, pp. 12274–12277, (2015).
15. Cherupurakal, Nizamudeen, R. Krishnapriya, Arjunkumar Bojarajan, Tholkappiyan Ramachandran, Sambasivam Sangaraju, Mohammad Sayem Mozumder, and Abdel-Hamid I. Mourad. "Enhanced electrochemical validation of metal organic frameworks-derived TiO_2/Fe-TiO_2 as an active electrode for supercapacitors." Materials for Renewable and Sustainable Energy 13, no. 3 (2024): 361-373.
16. Z. Wang, Z. Wang, Y. Pang, X. Wang, Y. Chen, Effect of Metal Substitution on the Optical Band Gap of MIL-125-NH_2, Chemistry Select 2023, 8, e202301509.